High-definition imaging of a filamentary connection between a close quasar pair at z = 3

Davide Tornotti [1]✉, Michele Fumagalli [1,2]✉, Matteo Fossati [1,3], Alejandro Benitez-Llambay[1], David Izquierdo-Villalba[1,4], Andrea Travascio[1], Fabrizio Arrigoni Battaia [5], Sebastiano Cantalupo[1], Alexander Beckett[6], Silvia Bonoli [7,8], Pratika Dayal[9], Valentina D'Odorico [2,10,11], Rajeshwari Dutta [12], Elisabeta Lusso [13,14], Celine Peroux [15,16], Marc Rafelski [6,17], Mitchell Revalski [6], Daniele Spinoso[18] & Mark Swinbank[19]

Filaments connecting haloes are a long-standing prediction of cold-dark-matter theories. Here we present a detection of the cosmic web emission connecting two quasar-host galaxies at redshift $z \approx 3.22$ in the MUSE Ultra Deep Field (MUDF), observed with the Multi Unit Spectroscopic Explorer (MUSE) instrument. The very deep observations unlock a high-definition view of the filament morphology, a measure of the transition radius between the intergalactic and circumgalactic medium, and the characterization of the surface brightness profiles along the filament and in the transverse direction. Through systematic comparisons with simulations, we validate the filaments' typical density predicted in the current cold-dark-matter model. Our analysis of the MUDF, an excellent laboratory for quantitatively studying filaments in emission, opens a new avenue to constrain the physical properties of the cosmic web and to trace the distribution of dark matter on large scales.

The existence of cosmic filaments connecting haloes hosting galaxies has been a long-standing prediction of theories describing a dark-matter dominated Universe. From earlier comparisons between N-body simulations and galaxy surveys, it has already become clear that models including pancake-like structures were superior in reproducing the observed galaxy distribution, hinting at the fact that galaxies trace an underlying mass distribution that extends beyond a few megaparsec[1]. Further development of simulations including baryons[2,3], the clustering analysis in ever-growing galaxy redshift surveys[4,5] and the ability of quasar spectroscopy to map the shadows of diffuse gas in absorption[6] have contributed to shaping our view of the intergalactic medium (IGM) as composed of a cosmic web: a network of filaments extending on megaparsec scales at the intersection of which dark matter overdensities become the cradles where gas collapses and forms galaxies.

Direct imaging of these filaments has proved challenging for several decades, as theoretical and numerical works predict that the filaments emit fluorescence radiation induced by ultraviolet background. In fact, the low intensity of the ultraviolet background[7] leads to an expected surface brightness (SB) emission of ~10^{-20} erg s^{-1} cm^{-2} arcsec^{-2} at redshift $z \approx 3$ (ref. 8), which is below the sensitivity limits of previous instruments. The deployment of large-format integral field spectrographs, such as the Multi Unit Spectroscopic Explorer (MUSE)[9] at the Very Large Telescope (VLT) and the Keck Cosmic Web Imager[10], has marked a breakthrough in studying the low SB Universe. Mapping gas around local ionizing sources, such as quasars, has become a routine experiment with multiple examples of ≫10^{-18} erg s^{-1} cm^{-2} arcsec^{-2} Lyα nebulae, typically on scales of a few hundred physical kiloparsecs (pkpc), known[11–15]. Among these examples, features approaching the megaparsec scale, as in the Slug Nebula[16], provided first hints of

filaments. More recently, the enhanced sensitivity has allowed us to obtain the images of patches of ionized gas stretching over scales of the order of ~1 pMpc (physical megaparsec) in a $z \approx 3.1$ galaxy protocluster[17] and to identify filamentary emission connecting galaxies[18]. Lyα emission from structures similar to bridges has also been observed around active galactic nuclei[19–21] and statistically detected in the intergalactic medium[22].

This work presents a detection and quantitative characterization of a cosmic web filament through its emission, at an SB of ~8×10^{-20} erg s^{-1} cm^{-2} arcsec^{-2}, connecting two massive haloes hosting quasars at $z \approx 3.22$ in the MUSE Ultra Deep Field (MUDF)[23,24]. The brighter quasar J2142−4420 has a continuum AB magnitude, $m_r = 17.9 \pm 0.02$ and systemic redshift $z = 3.221 \pm 0.004$; the fainter quasar J2142−4419 has $m_r = 20.5 \pm 0.03$ and systemic redshift $z = 3.229 \pm 0.003$ (ref. 25). The MUSE data, totalling 142 h on-source, allow us to image in high definition the entire emitting structure, which stretches for ~700 pkpc between and sideways of the two haloes. The data quality enables a detailed investigation of the Lyα emission from the IGM for more than 250 pkpc beyond the virial radii, at the low surface brightness predicted for cosmic filaments. With this data, we were able to map the Lyα surface brightness profile along the filament's spine and in the transverse direction. Finally, comparisons with numerical simulations offer insight into the typical density of cosmic filaments, a main prediction of the current cold-dark-matter models.

Previous analysis of a partial dataset of ~40 h (ref. 25) uncovered extended Lyα nebulae in the circumgalactic medium (CGM) of the quasar hosts, with asymmetric extensions along the direction of the two active galactic nuclei. Based on these features that indicated a gaseous bridge, we searched the region across the two quasars for low SB Lyα emission by selecting groups of connected pixels with a signal-to-noise ratio (S/N) above a threshold of 2 (see Methods for further details). This exercise identified Lyα emission in a connected region of ~30×90 arcsec^2. Figure 1 shows the optimally projected SB map of the connected emission, along with labels for the two quasars, QSO1 (the brighter) and QSO2 (the fainter). Table 1 summarizes the main properties of the emitting structures.

An extended emission stretches for over 700 pkpc in projection, both in the opposite and the in-between directions of the two quasars. With a mean surface brightness of 8×10^{-20} erg s^{-1} cm^{-2} arcsec^{-2}, the filamentary structure between the two quasars would not have been detected in shallower data acquired by most surveys reaching $\gg 10^{-19}$ erg s^{-1} cm^{-2} arcsec^{-2}. We confirmed the emission by extracting spectra from different regions along the main filament (boxes B, C and D in Fig. 1 and Extended Data Fig. 1). The map also revealed protuberances and smaller substructures branching from the main filament. Some of these substructures lie in regions of moderate depth due to the non-uniform sensitivity of the map (see, for example, box G in Fig. 1 and Extended Data Fig. 1), but the two largest protuberances—one extending sideways from the central part of the main filament to the west (box F) and the other from the nebula of QSO2 to the southwest (box A)—are spectroscopically confirmed. The general morphology of the system, composed of galaxies, nebulae and filaments, is remarkably similar to the configuration of galaxies assembling inside the cosmic web predicted by modern cosmological simulations[26,27]. Direct evidence of narrow filaments protruding from haloes is also reminiscent of the cold-mode accretion proposed by numerical simulations[28,29], as also seen in previous observations[30,31].

The depth of the MUSE observations in the MUDF provides sufficient data to analyse the structural properties of the filament. Starting with the flux-conserving projected surface brightness map obtained by collapsing the MUSE datacube in a wavelength window of 30 Å centred on the wavelength at the redshift of the Lyα emission peak, we extracted the Lyα surface brightness profile along the axis connecting the two quasars. We adopted a circular geometry and derived the azimuthally average profile for the emission arising in the nebula
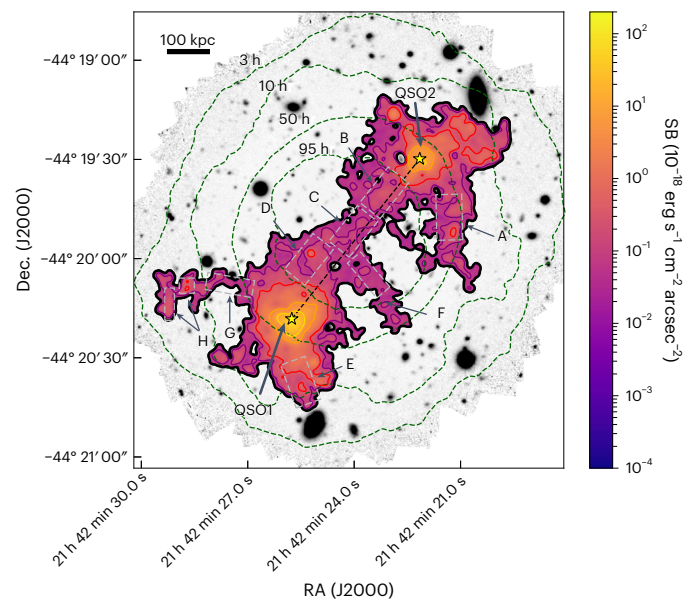

Fig. 1 | Lyα image of the filament in the MUDF. Optimally extracted Lyα image of the extended nebulae surrounding the two quasars (marked by yellow stars and the respective labels QSO1 and QSO2) and of the filament connecting them along the diagonal direction (dashed black line, ~500 pkpc). The contour levels are 0.02, 0.1, 0.4, 3.2 and 10×10^{-18} erg s^{-1} cm^{-2} arcsec^{-2} (black, purple, red, orange and gold, respectively). The black contour is the detection limit at S/N = 2. The colour bar covers the same values of Fig. 4. The dashed grey boxes labelled A to H are the same in Extended Data Fig. 1. The background, in grey, is a white-light image of the region imaged by MUSE, with the dashed green contours defining the exposure time map of the field according to the labelled values.

near the quasars. For the filament emission, we extracted, instead, the average surface brightness along the axis connecting the quasars inside rectangular regions (see Extended Data Fig. 2 for details). The central region within ~15 kpc of each quasar was excluded from the analysis owing to the residual of the quasar point spread functions, which have been subtracted from the original cube. The emission extracted from the nebulae and the filament profile joined smoothly, and we used the radius at which they intersect to switch from one geometry to another (see Methods for a detailed explanation).

The resulting profiles are shown in Fig. 2a on a linear scale and in Fig. 2b on a logarithmic scale to highlight better the profile of the quasar nebulae at small radii. The profiles rapidly decline with radius, following a power law with index ~−3.3 for Nebula 1 and ~−2.7 for Nebula 2 (see Methods for details on the fitting procedure) before reaching a plateau of almost constant SB in the region dominated by the filament emission. The profile near QSO2 appears to be a scaled-down version of that centred on QSO1. As shown in Fig. 2b, the radial profile measured for the two nebulae was entirely consistent in shape and normalization with the average profiles obtained for bright (median i-band magnitude 17.81 in ref. 13 and 18.02 in ref. 14) and faint quasar samples (median i-band magnitude 21.32 in ref. 32). Hence, the MUDF quasar nebulae are typical under this metric.

A slope change is apparent at larger radii when the profiles reach an SB of $\lesssim 10^{-19}$ erg s^{-1} cm^{-2} arcsec^{-2}. We attribute this variation in the power-law index to the transition between the regime dominated by the CGM of the quasar-host galaxies and the IGM. This is similar to the analysis performed in a nearby galaxy by Nielsen et al.[33] to infer the transition between the interstellar and circumgalactic medium. By modelling the full profile with a double power law (equation (1) in Methods), we constrained the transition radius between these two regions, R_t. For QSO1, $R_t = 117 \pm 8$ kpc, whereas for the fainter quasar QSO2 $R_t = 107 \pm 10$ kpc (Table 2). Values of ~100 pkpc are comparable to the virial radius of

Table 1 | Global Lyα properties of the two nebulae and the filament

	Area	Mean SB	Integrated flux	Size
	(arcsec^2)	(10^{-19} erg s^{-1} cm^{-2} arcsec^{-2})	(10^{-16} erg s^{-1} cm^{-2})	(pkpc)
Nebula 1	635[a]	17.4±0.1	11.1±0. 1[a]	117
Nebula 2	530[a]	7.1±0.1	3.78±0.05[a]	108
Filament	830[a]	0.83±0.06	0.69±0.05[a]	250

The nebulae properties are computed using circular apertures up to the transition radius between the CGM and IGM and centred on the quasar. This transition radius also defines the size of the nebulae. The properties of the filament were calculated using a box between the two nebulae, at a distance given by the transition radii. The length of this box defined the reported size of the filament. Data are reported as weighted averages along with their standard errors. [a]These quantities depend on the selected analysis region (Extended Data Fig. 2).

haloes with mass ~2–3 × 10^{12} $M_\odot$, which is the estimated halo mass of $z ≈ 3$ quasars at these luminosites[15,34]. Our analysis, therefore, provides an example in which the transition radius between the CGM and IGM is directly measured in emission at $z ≈ 3$. For comparison, at lower redshift ($z < 0.5$), using absorption line statistics and by measuring the covering fraction of H I absorption, Wilde et al.[35] found a typical size of about twice the virial radius for the CGM of star-forming galaxies.

We further compared the SB of the MUDF filament with the radial profiles in Lyman-alpha emitter (LAE) stacks by refs. 36,37 (dotted lines). Flattening at large radii is also evident in these cases (Fig. 2b), which can also be interpreted as the halo transition radius, which appears at smaller radii (40–60 kpc). However, in stacks, it is more challenging to disentangle the contribution of diffuse gas emission from filaments and the overlapping signal of additional haloes. Moreover, we observed a difference in SB by a factor of up to ten and even greater if we consider the SB levels <10^{-20} erg s^{-1} cm^{-2} arcsec^{-2} reached in the ultradeep stacked profile of ref. 38 at radii ≳50 kpc. These differences could be explained by the different halo mass scales investigated ($10^{12.5}$ $M_\odot$ for quasars and $10^{10–11}$ $M_\odot$ for LAEs) and by a different ionizing field. Moreover, the stacking technique introduces signal dilution due to geometric effects. Thus, our study provides a complementary and more direct view of filaments at the mass scale of $10^{12.5}$ $M_\odot$.

The quality of the MUDF data further allows the measurement of the filament properties in the direction transverse to that connecting the quasars (that is, the spine). For this analysis, we employed rectangular extraction regions outside the quasar CGM ($R > R_t$) and measured the average SB profile on both sides of the filament's spine (Extended Data Fig. 2). Both sides produced a comparable measure that we averaged to construct a final transverse Lyα profile (Fig. 3). In the transverse direction, the profile dropped with a power-law index of ~−0.74 up to ~70 pkpc. The total thickness was ≲2 × 70 ≈ 140 pkpc at the depth of our observations. There is no strong evidence in the current data of a clear edge or a change in the profile slope.

Finally, the observed SB is indicative of low-density gas ($n_H ≲ 10^{-2}$ cm^{-3}) inside the filaments. Adopting simple scaling relationships (see, for example, ref. 39) for a denser optically thick medium, we would obtain SB levels two orders of magnitude higher than those observed, given the quasar luminosities and the distance at which the filament lies. By contrast, the quadratic dependence of the emissivity in an optically thin recombination scenario (Methods), puts the characteristic density of the filament at ~5 × 10^{-3} cm^{-3} for the mean observed SB. However, in light of additional radiative processes and a density distribution within the emitting medium, a more refined inference on the gas density requires modelling of hydrodynamic simulations, as done in the next paragraphs.

The MUDF was selected for observations because of a pair of bright close quasars. To understand whether the properties derived from the MUDF filament can be generalized to other cosmic environments, we assessed how typical this double-quasar system is expected to be in a cold-dark-matter Universe.

For this task, we searched for MUDF twins in the semianalytic model (SAM) L-Galaxies based on the Millennium simulation[40,41] (see

Methods for further details). We opted for this model as it implements detailed quasar physics that successfully reproduces key statistics of the quasar population, including the observed luminosity functions reported in the literature. By selecting simulated quasar pairs within 0.3 dex of the observed bolometric luminosities (~2 × 10^{47} erg s^{-1} for QSO1 and ~2 × 10^{46} erg s^{-1} for QSO2 (ref. 42)) with projected distances of 400–600 pkpc and line-of-sight velocity separation of $\Delta v ≤ 1{,}000$ km s^{-1} (as estimated from the redshift of the quasars; see Methods), we found that the three-dimensional (3D) physical distance of pairs was closer than 2.5 pMpc for 95% of the systems and less than 1 pMpc in half of the cases (Extended Data Fig. 3).

With this SAM, we also inferred a number density of quasar pairs of 5.6 × 10^{-9} cMpc^{-3}, which implies an expected occurrence of one MUDF-like quasar pair within a volume of 560 cMpc^3. Using these twins, we derived the distribution of halo masses of bright and faint quasars (Extended Data Fig. 4), from which we inferred a typical halo mass of $\log(M_{vir}/M_\odot) = 12.91^{+0.34}_{-0.33}$ for the brighter quasar and $\log(M_{vir}/M_\odot) = 12.25^{+0.46}_{-0.35}$ for the fainter one. These halo mass values are consistent with current estimates of quasar hosts at comparable redshifts[15,34]. As we have no reason to expect that the underlying total hydrogen density distribution within the filament depends critically on the presence of quasars, we could use the halo mass distributions obtained from the SAM to select pairs with separations of ≲1 pMpc and investigate further with cosmological hydrodynamic simulations how filaments connect them.

For this analysis, we used the intermediate resolution simulation publicly available from the IllustrisTNG project (TNG100-1; see Methods and ref. 43), representing a compromise between resolution and volume. Within this box, we identified 144 pairs with halo masses given by the SAM, with a projected distance in the range of 400–600 pkpc and a 3D distance below 1 pMpc. First, we observed that these pairs are generally physically connected by a dense filamentary structure in contrast with pairs that have larger physical distances >2 pMpc. A thorough inspection of the simulated pairs revealed that the median density profile along the direction that connects the two haloes (Methods) declined from the central regions and smoothly reached a plateau with a minimum value of ~$10^{-3.7}$ cm^{-3}, that is, more than ten times the average cosmic density at these redshifts (~1.4 × 10^{-5} cm^{-3}). By contrast, for pairs with a physical distance >2 pMpc, the minimum value of the median profile reached ~$10^{-4.8}$ cm^{-3} (Extended Data Fig. 5), not far from the mean density. Along the filament's axis for connected pairs, the hydrogen density reached a median peak value of $10^{-2.8}$ cm^{-3} (see the transverse profile in Extended Data Fig. 6), indicating the presence of a denser spine in the central part of the cosmic web. Given these properties, we inferred that a typical filament with uniform hydrogen density of ~10^{-3} cm^{-3} and a radius of ~75 pkpc would have a total hydrogen column density of ~3–5 × 10^{20} cm^{-2}. Such a low-density gas exposed to ionizing radiation is predicted to have a neutral fraction ≲10^{-4}. We expect a neutral hydrogen column density below those of Lyman-limit systems ($N_{H I} < 10^{17.2}$ cm^{-2}), which is expected for absorption line systems in the IGM.

As two of the main Lyα emission mechanisms (recombination radiation and collisional excitation) depend quadratically on density,
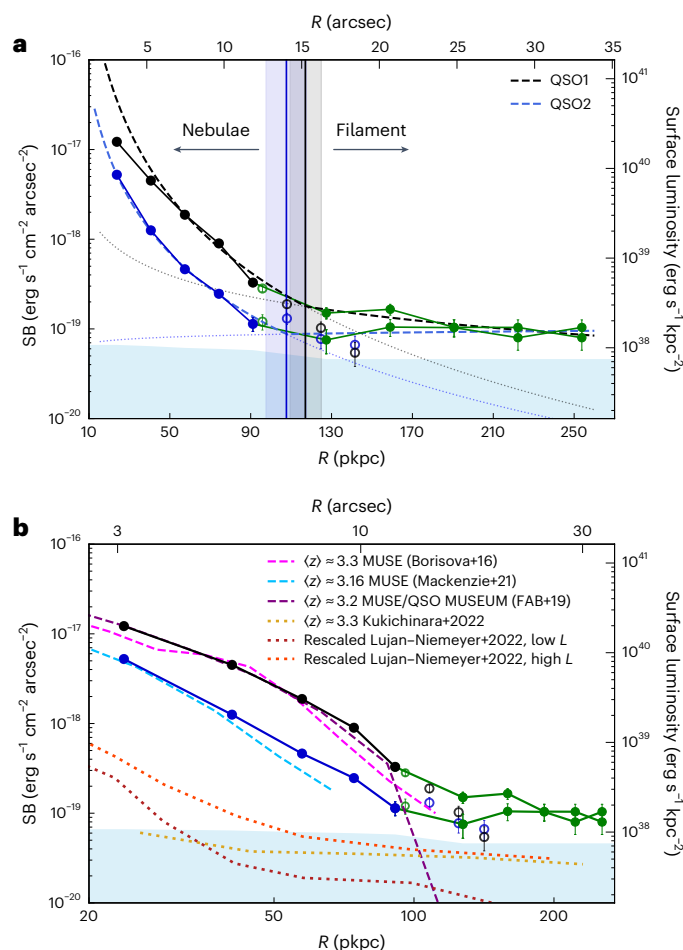
Fig. 2 | The Lyα SB profiles of the nebulae and filament. a, The extended Lyα emission's SB at the positions of QSO1 (black solid line) and QSO2 (blue solid line) are shown with filled dots, along with the filament profile (green solid line). The empty dots are the remaining data points measured using the different apertures (Methods). All points represent weighted averages along with their standard errors. The dashed lines (black and blue) represent the best-fit double power-law models. The two vertical solid lines (black and blue) denote the median values, along with the 16th and 84th percentiles, of the transition radii that separate the quasars' CGM from the filament. The dotted black and blue lines represent the extrapolation of the single power laws of the fitted function. **b**, Comparison between the measured SB profiles shown as in **a** but in log–log scale and literature profiles (dashed lines) in samples at comparable redshift and quasar magnitudes (see the text). The dotted lines represent stacked profiles around LAEs. The horizontal sky-blue region in both figures marks the NB detection limit (see Methods for the definition).

Table 2 | Best-fitting parameters for the SB profiles of QSO1 and QSO2

Parameter	QSO1	QSO2
R_t (pkpc)	117±8	108±10
A (10^{-18} erg s^{-1} cm^{-2} arcsec^{-2})	0.18±0.04	0.09±0.03
b_1	−3.3±0.1	−2.71±0.03
b_2	−0.9±0.3	0.1±0.4

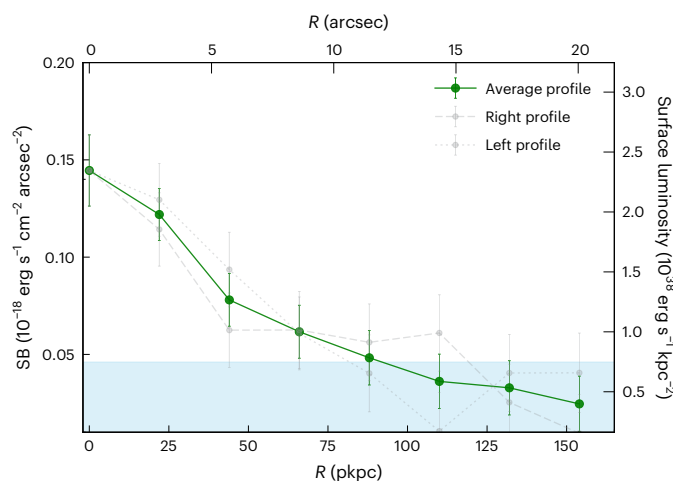Data are reported as median values, along with the 16th and 84th percentiles.

Fig. 3 | The transverse Lyα SB profile of the filament. The dashed and dotted grey lines represent the right and left profiles relative to the direction connecting QSO1 with QSO2. The green solid line shows the resulting average profile combining the two. All points represent weighted averages along with their standard errors. The horizontal sky-blue region marks the NB detection limit (see Methods for the definition).

a comparison between the observed and predicted SB of filaments offers a way to constrain the typical order of magnitude underlying gas density within the filaments. We computed SB maps (see a full description in Methods) under the approximation where recombinations and collisional excitations give the total emissivity of the diffuse gas, that is, below the densities at which the gas in the adopted model lies on the imposed equation of state ($n_H < 0.1$ cm^{-3}). We do not include scattering in this baseline model, but note that radiative transfer calculations imply a boost factor of 2–3 (ref. 44) at the observed SB levels. Hence, our main conclusions about the inferred density are not substantially affected. Owing to the presence of the quasars and to test their possible effects, we also considered a maximal fluorescence model, in which bright sources fully ionize the gas that emits only through recombination. We find that at the typical densities of the filaments, the gas is already substantially ionized, and the maximal fluorescence model does not differ significantly from the baseline calculation (Methods). Finally,

we also studied the resolution effects by repeating the same analysis in other boxes of the TNG suite (TNG50-1 and TNG300-1) for a factor of ~200 in resolution (Methods). The predicted SB is generally insensitive to the resolution adopted for the simulations. Although large clumping factors (up to ~1,000 (ref. 16)) are often invoked to reproduce the high SB of the quasar nebulae, such as the Slug Nebula, in the low-density regime of the MUDF filament, clumps do not appear essential to reach the observed SB levels. A low filling factor of optically thick clouds within filaments is also in line with the statistics inferred from the absorption lines and the prediction of simulations of the Lyα forest.

Considering our baseline model and following the same methodology adopted in the MUDF analysis, we calculated the median transverse SB profile of filaments between pairs (Extended Data Fig. 7). The observed and simulated profiles shared a different normalization. However, raising the density of the filaments by less than a factor of three would be enough to match the observed profile, considering the contribution of recombinations alone. A further contribution from collisions reduces this discrepancy, which could even be removed if an $n_H > 0.1$ cm^{-3} gas is considered (Methods), or by allowing for a moderate boost from scattering. Finally, owing to intrinsic differences in the various simulated profiles, we could identify close matches in terms of the transverse SB profile of the MUDF filament inside this simulation. An example of this is shown in Fig. 4.

From this comparison, we concluded that the typical density inferred from the cosmic web in these simulations must be of the order of what is found in the MUDF filament and, at present, there are no obvious indications of discrepancies between observations and the predictions of the cosmic web in the adopted cold-dark-matter model. Our
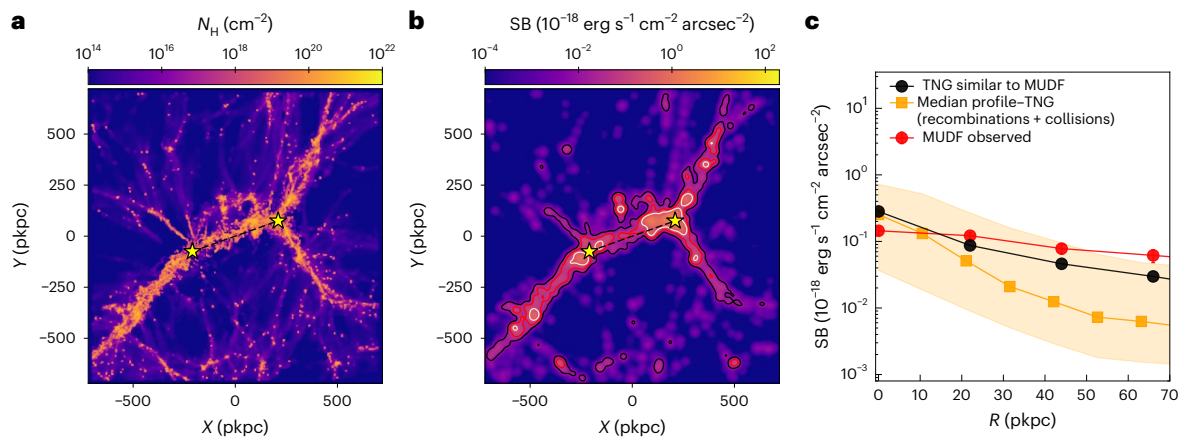
Fig. 4 | Simulated pair similar to the one in MUDF. a,b, Example of a simulated pair with a 3D physical distance below 1 pMpc, closely resembling the MUDF system. **a,** The hydrogen column density map. **b,** The SB map, smoothed on the same scale as the reconstructed MUDF maps. Contour levels of 10^{-20}, 10^{-19} and 10^{-18} erg s^{-1} cm^{-2} arcsec^{-2} are marked (black, red and light-yellow lines, respectively). **c,** The transverse SB profile of the MUDF twin (black line) compared with the MUDF data (red line). Also shown is the median transverse profile obtained with the pairs with a 3D distance below 1 pMpc (yellow line with shaded regions marking the 16th and 84th percentiles). The profile is shown up to ~70 pkpc, where the measurements exceeded the detection limit.

study, which has offered quantitative measurements of the structural properties of the cosmic filaments at $z \approx 3$ beyond a simple detection, exemplifies a tantalizing new direction for constraining the cosmic web with quantitative data to deepen our understanding of one of the most fundamental predictions of the cold-dark-matter model.

The remarkable depth, with a detection limit in the deepest part of the NB image of 4.5×10^{-20} erg s^{-1} cm^{-2} arcsec^{-2} reached by the MUDF observations enabled the detection of a prominent cosmic filament that connects two haloes hosting quasars at $z \approx 3.22$. These observations facilitate a high-definition view of the cosmic web, which allows us to characterize the filament morphology and directly measure the transition radius between the IGM and the CGM, which occurs around the virial radius for ~2–$8 \times 10^{12}\ M_\odot$ haloes. We also derived the SB profile along the filament and in the transverse direction. With the aid of SAM and cosmological hydrodynamical simulations, we have shown how the MUDF field is an excellent laboratory for studying the physics of general filaments around $\gtrsim 10^{12}$–$10^{13}\ M_\odot$ haloes at $z \approx 3$. Our analysis reveals that a main filament, with gas overdensities above ten times the mean cosmic density, connects most haloes with physical separation <1 pMpc. This differs from what is seen in pairs at larger separations, for example >2 pMpc, where the gas between haloes drops to the mean density.

By exploiting the quadratic dependence of the Lyα emissivity for two main channels of photon production (recombination and collisional excitation), we have used the observed SB maps to test the predicted density distribution of cosmic filaments in the current cold-dark-matter model. We found a shift between the simulated and observed Lyα SB levels. However, this difference can be easily removed by raising the underlying density of the filaments by less than a factor of three, which demonstrates that the typical densities in models are within acceptable values. Moreover, we identified examples inside the simulation that closely match the observed MUDF system. Therefore, the current data do not highlight significant tensions with the cold-dark-matter model.

By moving from detections to quantitative analysis of the cosmic web, our study demonstrates the exciting potential of spectrophotometry of cosmic filaments for testing how cosmic structures assemble. As the cosmic web is a fundamental prediction of the current cosmological model, a quantitative characterization of its structure and physical properties should be explored more, as a way to test the nature of dark matter. Building on our work, future ultradeep observations of cosmic filaments in the era of 40 m telescopes coupled with sophisticated numerical models will strengthen our understanding of the Universe in new ways.

Methods

Observations and data reduction

Observations of the MUSE Ultra Deep Field (RA = 21 h 42 min 24 s, dec. = −44° 19' 48'') were obtained as part of the European Southern Observatory Large Programme (PID 1100.A−0528; Principal investigator, Fumagalli) in periods 99–109, using the MUSE instrument in wide-field mode with extended wavelength coverage in the range $\lambda = 4{,}650$–$9{,}300$ Å. A total of 358 individual exposures were collected. Each exposure was dithered around the nominal pointing centres, positioned on the line connecting the two QSOs, and rotated in steps of 5°. The last 60 exposures were centred at six positions surrounding the QSOs, to slightly extend the footprint of the final mosaic at the same time as collecting more depth in the central region. This approach, combined with advanced illumination correction algorithms[24,45,46], reduces the instrumental signatures in the final coadd produced by the different response of the 24 MUSE spectrographs. Each exposure had an integration time of 1,450 s except for the first 19, which were integrated for 1,200 s, leading to a total observing time of 142.8 h on-source. The final mosaic covered an area of ~1.5×1.5 arcmin^2, with maximal sensitivity in the inner of ~1 arcmin^2 region (Fig. 1). Using the GALACSI adaptive optics system improved the image quality compared with natural seeing, yielding a full-width at half-maximum of ~0.73 arcsec for point sources.

The reduction of MUSE data followed the steps described in the MAGG survey[46] and articles in the MUDF series[24]. Using standard techniques from the MUSE pipeline (v.2.8 (ref. 47)), we corrected the raw data for primary calibrations (bias, dark, flat correction, and wavelength and flux calibration). Next, individual exposures, sky-subtracted and corrected for residual illumination using the CubExtractor toolkit (v.1.8, CubEx hereafter; see ref. 45 for further details), were coadded, without weighting, in a final datacube with a pixel size of 0.2 arcsec and 1.25 Å in the spatial and spectral direction, respectively. Before the final coaddition, the pixels at the edges of the slitlets, which were affected by slight vignetting, were masked and each exposure was inspected. In two exposures, satellite trails were encountered and masked. An associated variance cube was also reconstructed using the bootstrap technique developed in previous work[24,46]. The final data achieved a depth of up to 110 h and a pixel root mean square of 3×10^{-21} erg s^{-1} cm^{-2} Å^{-1} pix^{-1} (at ~5,200 Å; see below), making this observation comparable to the MUSE eXtremely Deep Field[18].

Owing to the exquisite sensitivity of these data and the fact that we are interested in extended low SB emission, we minimized the impact

of small sky residuals by performing a final correction of the background level. For this, we selected pixels in regions empty of continuum sources and far from where we expect Lyα emission. After identifying the extended emitting structure in the datacube (see next section), we explicitly checked that no source contribution was contained in these sky regions. Next, we constructed a median sky spectrum over ~5,000 pixels and used this spectral template for the final sky subtraction. Locally, this template was normalized to the residual sky values measured in two narrow-band (NB) images of spectral width 60 Å, which we selected around $\lambda = 4,800$ Å and $\lambda = 5,400$ Å, far enough from the wavelength interval where we expect Lyα emission at $z \approx 3.22$. Ultimately, we achieved robust sky subtraction, where the residual level was <1% of the pixel root mean square measured in the deepest central region of the field of view (>95 h) and in the spectral ranges 4,900–5,100 Å and 5,200–5,400 Å that were adjacent to the wavelengths where we expected Lyα emission.

Identification and extraction of the filament and nebulae

The presence of two bright Lyα emitting nebulae around the two MUDF quasars has been already confirmed in a partial, ~40 h, dataset by Lusso et al.[25]. To search for more extended and very low SB emission in the datacube, we used the CubEx tool to subtract continuum-emission sources and the quasar point spread function through a non-parametric continuum-subtraction algorithm (see refs. 14,45 for further details). Next, we identified groups of >2,500 connected voxels above a S/N threshold of 2, with a minimum number of 500 spatial pixels. To increase the sensitivity to low SB emission, we further smoothed the cube with a Gaussian kernel with a size of 3 pixels (0.6 arcsec or 4.6 pkpc) in the spatial direction, masking continuum sources to avoid contamination from negative or positive residuals created during the continuum-subtraction process. No smoothing was applied in the wavelength direction to maximize the spectral resolution. We also demanded that at least three wavelength layers be connected in the spectral direction to avoid spurious thin sheets of emission.

This search yielded two connected and very extended structures (>30,000 voxels). One of them covered the two quasars, with the brightest emission coinciding with the quasar positions. The other was the previously known Nebula 3 at a different redshift of 3.254 in ref. 25. The quasars' Lyα nebulae were detected to an SB limit of ~1×10^{-19} erg s^{-1} cm^{-2} arcsec^{-2} in the new data. With ultradeep observations in the central region, we also uncovered a filamentary and extended emission signal that originated from the edges of the quasar nebulae and connected them in the direction of the putative filament proposed in ref. 25. Additional extended emission was detected in the opposite direction for both quasars, suggesting that the emitting structure extends for more considerable distances than probed by our data. The detection of the nebulae and filaments with their overall morphology does not depend on the selection criteria described above. In fact, we performed the extraction using different S/N thresholds (up to 2.5) and different spatial (2 and 4 pixels) and spectral (0 and 1 pixel) smoothing settings, all of which yielded the same global emission structures when the different parameters employed were considered.

The detected signal was then projected along the wavelength direction to compose an optimally extracted Lyα image, shown at the top of the white-light image in Fig. 1 and at the top of three collapsed wavelength layers at the central wavelengths of the nebulae to assess the background noise level in Extended Data Fig. 1. Optimally extracted maps are best suited to highlight low SB emissions. However, as they combine only the voxels identified by CubEx above the S/N threshold as harbouring significant emission, they may lose flux and are inadequate for precise estimates of the total SB (see, for example, ref. 13). Therefore, we resorted to a synthesized NB image centred on the wavelength at the redshift of the Lyα emission peak and obtained by summing the flux in the wavelength direction over 30 Å for all the measurements presented in this work. Hereafter, we use the term Nebula 1 (Nebula 2)

to refer to the one associated with the brighter (fainter) quasar, QSO1 (QSO2), as indicated in Fig. 1.

Although the nebulae were detected at high S/N, the extended low SB signal across the filament, with ~8×10^{-20} erg s^{-1} cm^{-2} arcsec^{-2}, was close to the detection limit of the NB image (~2σ; see the section 'Analysis of the SB profiles' for how the detection limit σ is defined in the NB image). Therefore, we performed a series of tests to confirm the genuine nature of the detection. First, we searched again for the detected signal in a primary data reduction before applying any illumination correction or enhanced sky subtraction using the CubEx code. Second, we verified the presence of the extended structure in two independent coadds containing each half of the total number of exposures. The filament was recovered in each test, although at lower S/N owing to the higher noise of the various products and methods used for this test. Finally, we verified that the signal along the main filamentary structure connecting the two quasars represented a significant spectral feature in the datacube. By masking pixels associated with continuum sources, we extracted the mean spectra from five distinct regions, which are labelled A, B, C, D and E, each measuring approximately 14×8 arcsec^2, and positioned along the main filament, extending from the vicinity of QSO2 up to QSO1, as illustrated in Extended Data Fig. 1a. Additionally, we considered three other apertures, labelled F and G, each ~20×8 arcsec^2, and H composed of two apertures of 7×7 arcsec^2 and ~15×4 arcsec^2, respectively, positioned along the thin protuberances branching from the main filament, as illustrated in Extended Data Fig. 1a.

In Extended Data Fig. 1b, we present the extracted normalized spectra for each extraction box. The spectra are shown in velocity space, with the reference zero velocity (marked by the vertical dashed blue line) calculated from the first moment of the line within a wavelength range ±10 Å around the Lyα emission peak. The dashed horizontal green line represents the 1σ noise level of the spectrum estimated from the wavelengths not in the interval of the Lyα emission. The spectra extracted in the regions along the main filamentary structure confirm that the detected signal was an actual emission of astrophysical origin and did not arise from spurious noise or systematic artefacts in the advanced processing of the data. In addition, we spectroscopically confirmed the presence of the protuberance in box F. Box G, including pixels connected to QSO1 by the algorithm, did not show a clear emission line at the present depth, but aperture H revealed a detectable signal, although it was more affected by noise.

Using these spectra, we also assessed the kinematic properties of the filament. We examined the first moments of Lyα emission lines extracted along the main filamentary structure using boxes A, B, C, D and E, comparing them to the wavelength at the redshift of the Lyα emission peak. No significant velocity gradient along the main filamentary emission structure was detectable, within the errors and at the present depth ($|\Delta v| < 100$ km s^{-1}). In Extended Data Fig. 1 we also mark the positions of the detected and spectroscopically confirmed LAEs within 1,500 km s^{-1} of the average systemic redshift of the two quasars with green crosses. In the main filamentary structure connecting the two quasars, where our analysis was focused, we identified only one LAE. Whenever we masked continuum sources, including during the spectra extraction, we also excluded compact emission from this LAE.

Analysis of the SB profiles

We computed the SB profiles of the nebulae associated with the two quasars and the filament from the synthesized NB image. Before extracting the SB profiles, we applied a mask to avoid residuals of the continuum subtraction of compact sources, which could introduce contamination. The percentage of unmasked pixels in each region used for the analysis was >80%. Subsequently, for each nebula, we computed the circularly averaged SB profile, using rings with an aperture of ~10 spatial pixels (equivalent to ~2 arcsec or ~15 pkpc), up to a radius of 150 pkpc centred at the positions of the quasars. In Extended Data

Fig. 2, solely for illustrative purposes, we overplot the annuli on the optimally extracted image within which we calculate the SB profiles (in black for Nebula 1 and blue for Nebula 2). We excluded a circular 2 arcsec² region around the quasars to avoid residuals from the point spread function subtraction (the two black dots). Hence, the radial profiles are presented for $R \gtrsim 15$ kpc. Instead, we used ten boxes for the filament, each with dimensions of approximately 20×80 pixels² along the direction connecting the two quasars, starting at a distance of 80 pkpc from them. These boxes are shown in green in Extended Data Fig. 2a.

To calculate the SB value for each annulus and box, we adopted a variance-weighted average of all unmasked pixels, consistently propagating the errors from the associated variance image. Detection limits were computed radially, taking into account the effective exposure time and the number of pixels in the regions considered for this analysis. We also explicitly verified that no residual background signal was detected in empty regions above the detection limit. Considering the varying aperture widths and shapes used and the irregular geometry of the emission, we examined the overlapping regions between the rings and the boxes to join the nebula and the filament profile. In Fig. 2a, the observed SB data points are shown using the same colours as for the extraction apertures in Extended Data Fig. 2a: black dots represent the measured values in the annuli for Nebula 1, blue dots represent those for Nebula 2 and green dots represent those for the boxes in the filament. The filled dots mark the combined SB profiles, whereas the empty dots are the individual aperture measurements not included in the final profile and up to the detection limit of the NB image.

The profile of both quasars was rapidly decreasing to radii of ~100 pkpc, which we identified as the Lyα nebulae arising from the CGM of the host. The plateau at ≥100 pkpc extending to 250 pkpc—the midpoint between the two quasars—instead arises from the filament. Examining the empty data points of the two nebulae above ~100 pkpc, the excess emission from the filament became evident compared with what was measured in the annuli. Clearly, the filament signal was also enclosed in the annuli, but the filling factor became progressively low as the radius increases, making this circular geometry a poor choice for the filament SB. Moreover, the annuli included the signal on the opposite side of the nebulae, where the filamentary structure was fainter, yielding a steeper profile.

In Fig. 2b, we compare the observed profiles of the two nebulae on a log–log scale with the average profile from the $z \approx 3.3$ sample of Borisova et al.[13] (dashed magenta line), the $z \approx 3.2$ sample of Arrigoni Battaia et al.[14] (dashed purple line) and the $z \approx 3.16$ faint sample of Mackenzie et al.[32] (dashed sky-blue line). We observed that both of our nebulae have a profile that is in excellent agreement with those in the literature at the same redshift, after accounting for the different magnitudes of each quasar. In fact, the i-band magnitudes of the quasars in the sample from ref. 13 range from 16.6 mag to 18.6 mag. Those of ref. 14 range from 17.4 mag to 19 mag and include in the sample the brighter QSO1, with an i-band magnitude of 17.6 mag. Finally, the i-band magnitude of the quasars in ref. 32 ranges from 20 mag to 23 mag, and is thus comparable with the fainter QSO2, with a magnitude of 20.6 mag in the same band. We conclude that both quasars have a typical CGM when traced by Lyα despite being in a close pair.

An evident inflection point is visible in both profiles around ~100 pkpc from the quasars, which we ascribe to the transition between the CGM traced by the quasar's nebulae and the IGM traced by the filament. To explore this transition more and to separate the emission of these two components, we fitted the complete SB profiles (filled dots) with the broken power-law model

$$SB(R; A, R_t, b_1, b_2) = \begin{cases} A\left(\dfrac{R}{R_t}\right)^{b_1} & \text{if } R \leq R_t, \\ A\left(\dfrac{R}{R_t}\right)^{b_2} & \text{if } R > R_t. \end{cases} \tag{1}$$

where R_t is the transition radius between the CGM and the IGM, A is the normalization, and b_1 and b_2 are the two slopes. The choice of a power-law function is justified in the quasar Lyα nebulae literature context (see, for example, refs. 13,14). To determine the best parameters, we employed a Bayesian approach, assuming a Gaussian likelihood for each SB estimate and a uniform prior. The best-fitting parameters obtained through the emcee algorithm[48] are reported in Table 2.

The best fits are shown in Fig. 2a as black and blue dashed lines for QSO1 and QSO2. The solid vertical lines, with the same colours, represent the transition radius and its error. Instead, the dotted black and blue lines represent the extrapolation of the best fit for the nebulae and the filament for each quasar, further confirming the presence of an emission excess in the filament region. This model thus recovers a natural transition between the CGM and the IGM in the range of ~90–130 kpc, with the fainter quasar having a smaller size of the Lyα-emitting CGM as observed in previous studies[32,49]. For typical halo masses in the order of ~$10^{12.3-12.5}\ M_\odot$ for these quasars[15,34], the virial radius at $z \approx 3.2$ is $R_{vir} = 92$–108 kpc, that is, comparable with the size of the transition radius. The transition occurs at an SB of ~$(1-2) \times 10^{-19}$ erg s⁻¹ cm⁻² arcsec⁻², with only a small difference with the quasar luminosity.

In Fig. 2b, we also compare the observed SB profile with stacked profiles of LAEs (dotted lines) obtained in refs. 36,37. A similar flattening at large radii was observed in these analyses, although at different radii (40–60 kpc). The mean Lyα luminosity of the LAEs studied by Kikuchihara et al.[36] at $z = 3.3$ is $\log(L_{Ly\alpha}/\text{erg s}^{-1}) = 42.5$ and the sample in Lujan–Niemeyer et al.[37] is divided in low ($\log(L_{Ly\alpha}/\text{erg s}^{-1}) < 43$) and high ($\log(L_{Ly\alpha}/\text{erg s}^{-1}) \geq 43$) luminosity, with a median $z = 2.5$. After rescaling by SB dimming[37], we observed that the SB profiles in Kikuchihara et al. and the sample in Lujan–Niemeyer et al. lie below the observed MUDF profile by a factor of 3–4 at high luminosity and up to a factor of 10 at low luminosity. Moreover, we observed that QSOs have a higher emission profile, in particular in the inner regions (that is, their CGM) than LAEs. This discrepancy can originate from the different halo masses probed (~$10^{12.5}\ M_\odot$ for quasars and $10^{10-11}\ M_\odot$ for LAEs) as well as different ionizing fields. A further explanation for the observed discrepancy at larger radii can derive from the stacking technique used, which was different from our direct measurement of a single structure connecting two massive haloes. Indeed, in stacks, there can be a signal dilution when coadding structures that are not fully aligned.

The depth and quality of the data also allowed us to extract the transverse SB profile of the filament. We calculated the weighted average value from boxes measuring ~160×14 pixels² each, up to a distance of 165 pkpc on the right and left sides relative to the direction connecting the two quasars. The 15 boxes were off-axis by 7 pixels in the northeast direction to capture the emission peak at $R = 0$. To account only for the filament emission and to avoid contamination from the two nebulae, the length of each box was determined by the distance from the two quasars, selected as the transition radius estimated above (Extended Data Fig. 2). The right and left SB profiles are shown in Fig. 3 with grey dashed and dotted lines, respectively. A solid green line shows the combined average profile. Fitting the profile in the region above the detection limit with a power law, we obtained a slope of -0.74 ± 0.15, and we observed that the transverse projected width of the filament extended up to approximately 70 pkpc without reaching a clear edge at the depths of our observations.

As the formal error does not fully account for the pixel covariance arising from the cube reconstructions[24], we calculated an empirical SB detection limit profile that considered the different extraction apertures and the varying mean exposure times within them. To achieve this, we extracted an NB image of 30 Å, shifted by approximately 60 Å from the Lyα peak wavelength emission. This spectral region was chosen because we did not expect any source emission. First, to determine the SB limit associated with the extraction box used for the profiles of the main filament, we focused on the central region of the field of view, specifically in the area with the deepest data (exposure time >95 h), in

which the emitting filament was detected. We obtained the distribution of the average SB values along 1,000 box apertures, masking any residuals of the continuum subtraction and requiring a percentage of unmasked pixels higher than 95%. The NB detection limit (1σ) was then defined as the standard deviation of the distribution above the mean value. To determine the SB limit associated with the extraction annuli used for the profiles that characterize the two nebulae around the quasars, we applied the same procedure described above, with the additional condition that the average exposure time of each randomly located annulus was within 10 h of the average exposure time of the reference annulus in the NB around the Lyα signal, which was ~60–65 h. The resulting detection limit profile is shown by the sky-blue region in Figs. 2 and 3. In the deepest region of the field, this detection limit reached 4.5×10^{-20} erg s^{-1} cm^{-2} arcsec^{-2}, ensuring that the measured Lyα SB profile was always statistically significant.

To measure the global properties of the detected emission, we used the transition radius as a reference to differentiate between the nebulae and the filament. The nebula around QSO1 has a total flux of ~1.1×10^{-15} erg s^{-1} cm^{-2} over a total area of ~635 arcsec^2, whereas the nebula around QSO2 has a total flux of approximately 3.8×10^{-16} erg s^{-1} cm^{-2} over a total area of ~530 arcsec^2. This led to a total luminosity of ~1×10^{44} erg s^{-1} for Nebula 1 and 3.6×10^{43} erg s^{-1} for Nebula 2. The total linear extension of the emitting structures was also calculated considering the projected distance between the two quasars and the projected distance up to ~1×10^{-19} erg s^{-1} cm^{-2} arcsec^{-2} on the opposite side of the filament, leading to ~700 pkpc. Table 1 summarizes these global properties.

The filament, considered up to ~70 pkpc in the transverse direction, had an average SB of approximately 8.3×10^{-20} erg s^{-1} cm^{-2} arcsec^{-2}, which was similar to the average levels of ~3.5–11×10^{-20} erg s^{-1} cm^{-2} arcsec^{-2} found in ref. 18 around groups of LAEs at $z \approx 3$–4. Given the observed SB level and the presence of two bright quasars, we could exclude the fact that the bulk of the emitting gas was optically thick, as simple scaling relations[39,50] would suggest much brighter emission. Instead, the observed signal aligned more closely with an optically thin scenario, a hypothesis that we will corroborate next using hydrodynamic simulations.

Analysis of the SAM model

As the MUDF was selected for the particular configuration of two closely spaced quasars, we aim to understand how common haloes traced by the two quasars are in a cold-dark-matter universe to assess whether the properties of the MUDF filament can be used to learn about the IGM connecting haloes at this mass scale. Thus, we turn to the analysis of SAMs with two objectives: to place our system in a broader cosmological context by assessing the expected number density of MUDF-like pairs and to infer the most probable distributions of dark matter halo masses of the MUDF quasars. With these distributions, we considered a hydrodynamic simulation to place constraints on the filament gas density.

For these tasks, we used a light cone generated with the updated version of the L-Galaxies SAM models[51], as detailed in refs. 40,41. These models were run using the subhalo merger trees from the Millennium[52] dark matter N-body simulation within a periodic cube of side 500 cMpc h^{-1}. The quasar phase of a galaxy is triggered by gas accretion onto black holes, and this model accounts in detail for these processes, reproducing statistics in good agreement with observations, including the literature quasar luminosity functions (see ref. 41 for a more comprehensive discussion). Therefore, we could leverage these models to identify systems similar to the MUDF.

Using the methodology presented in ref. 40, we created a light cone covering the full sky in the redshift range $z \approx 2.8$–3.8, which was centred on the mean redshift of the two MUDF quasars ($z \approx 3.22$). Next, we selected the bright quasars corresponding to QSO1 with a bolometric luminosity of $\log(L_{bol}/\text{erg s}^{-1}) = 47.3 \pm 0.3$ and the faint sources

corresponding to QSO2 with luminosity $\log(L_{bol}/\text{erg s}^{-1}) = 46.3 \pm 0.3$ (ref. 42). This resulted in a number density of approximately 3×10^{-7} cMpc^{-3} and 8×10^{-6} cMpc^{-3}, respectively. The virial mass distribution for the two samples had a mean value of $\log(M_{vir}/M_\odot) = 12.79^{+0.34}_{-0.32}$ for the bright sample and $\log(M_{vir}/M_\odot) = 12.20^{+0.40}_{-0.30}$ for the faint sample. The errors represent the 16th and 84th percentiles of the distributions. These frequency distributions are shown as grey histograms in Extended Data Fig. 4 and are normalized to the total number of bright and faint sources selected, respectively.

To obtain systems that mimic the MUDF quasars in the sky, we selected all pairs separated by a projected physical distance in the range 400–600 pkpc, encompassing the projected separation observed for the MUDF pair. The selection led to a pair density of ~3×10^{-8} cMpc^{-3}. We also included the redshift information by relying on optical rest-frame spectroscopy of the two MUDF quasars. Noting that the actual separation in velocity space for the MUDF pair was $\Delta v = 568 \pm 355$ km s^{-1}, we required that the selected pairs had $\Delta v \leq 1{,}000$ km s^{-1}, resulting in a number density of 5.6×10^{-9} cMpc^{-3}. Thus, to find at least one pair similar to those in the MUDF, we needed to sample a cube volume with a comoving side of ~560 cMpc, which is ~75% of the comoving side of the cube used in the Millenium simulation. The configuration of the MUDF is thus rare but not highly uncommon in the high-redshift Universe.

The pairs' virial halo mass frequency distributions under this final selection are shown in Extended Data Fig. 4 (red and blue curves for the bright and faint quasars). The mean values are $\log(M_{vir}/M_\odot) = 12.91^{+0.34}_{-0.33}$ for QSO1 and $\log(M_{vir}/M_\odot) = 12.25^{+0.46}_{-0.35}$ for QSO2. As above, the errors represent the 16th and 84th percentiles of the distributions, which we normalized to the total number of bright and faint sources obtained after the final selection. The mean masses were slightly larger than those obtained using only the bolometric luminosity selection, as imposing stringent constraints on the physical distance between haloes allowed us to preferentially select more biased regions than random pairs. We then derived the underlying 3D physical distance distribution, as shown in Extended Data Fig. 3, and the cumulative distribution function (red line); 95% of the systems were closer than 2.5 pMpc and more than 50% were closer than 800 pkpc. Thus, a large fraction of pairs in the MUDF configuration were part of the same large-scale structure and could be interacting in some form.

Analysis of hydrodynamic simulations

With the mass distribution of the MUDF pair in hand, we considered hydrodynamic cosmological simulations to explicitly verify the hypothesis that gaseous structures physically connect systems similar to the MUDF pair twins. We considered the IllustrisTNG simulations[43], focusing specifically on TNG100-1, which was the intermediate periodic simulation box of side length ~100 pMpc. With a gas particle mass of $1.4 \times 10^6 M_\odot$ and a dark matter particle mass of $7.5 \times 10^6 M_\odot$, TNG100-1 balances volume and resolution. Each TNG simulation included a comprehensive model for galaxy formation and solved the coupled evolution of dark matter, cosmic gas, luminous stars and supermassive black holes from $z = 127$ to $z = 0$. The simulation generated several snapshots across cosmic time and, for our analysis, we considered the one at redshift $z = 3.28$, which is similar to the redshift of the MUDF system.

Using the halo mass distributions of the pairs similar to MUDF obtained from SAM (Extended Data Fig. 4), we selected a sample of pairs within TNG100-1 with halo masses matching those of each SAM pair within 0.1 dex. We required a projected physical distance in the range 400–600 pkpc and a 3D distance below 5 pMpc, according to the 3D physical distance distribution of the SAM in Extended Data Fig. 3. We analysed separately two distinct regimes: pairs with a 3D distance below 1 pMpc (144 close pairs) and those at a larger distance, above 2 pMpc (52 distant pairs).

We calculated the hydrogen density profile for each pair along the direction that connects the haloes, considering all gas resolution elements within a cylinder positioned between the two haloes. The axis

of the cylinder corresponded to the line connecting the two haloes, and the radius of the cylinder was set to 100 pkpc to encompass potential filamentary structures in between. We verified that this geometry fully encompassed the filaments in nearly the entire sample. After normalizing the length of the cylinder by the 3D physical distance of the pair, we divided it into 15 uniformly distributed slices to ensure a sufficient sampling of the profile. We verified that alternative slice choices did not affect the results. For each slice, we computed the hydrogen density as the total mass contained in the slice divided by the volume of the slice, assuming a primordial hydrogen fraction $X_H = 0.76$.

The median density profiles of the pairs, both those with a 3D distance below 1 pMpc and those above 2 pMpc, are shown in Extended Data Fig. 5. The sky-blue and orange-shaded regions mark the 16th and 84th percentiles of the profile distribution, respectively. Pairs with a 3D distance below 1 pMpc are typically connected by a denser medium (see, for example, Fig. 4a), exhibiting a smooth transition from the CGM to the IGM, with a minimum median hydrogen density value of ~$10^{-3.7}$ cm^{-3}. By contrast, distant pairs with a 3D distance above 2 pMpc are not typically connected by an identifiable overdense structure and display a steeper radial hydrogen density profile, reaching a minimum median hydrogen density of ~$10^{-4.8}$ cm^{-3}. We interpret this result as statistical evidence of more overdense filaments connecting the close pairs. To further quantify the occurrence of connecting filaments between the two subsamples, we also calculated the hydrogen density within a cylinder of radius 100 kpc in the region ranging from $0.25d_{3D}$ to $0.75d_{3D}$, focusing solely on the contribution of the filamentary structure and excluding the region associated with the CGM. We determined the fraction of pairs with a filament density value above a threshold of ten times the critical hydrogen density at redshift ~3.22, which is ~1.4×10^{-5} cm^{-3}. This reference value aligns with the strongest absorbers observed in the Lyα forest from quasar spectra (see, for example, ref. 6). Most systems with a 3D distance below 1 pMpc (75%) exhibit densities exceeding this threshold, whereas only 8% of systems with a 3D distance above 2 pMpc exceed this threshold. We thus concluded that the former subsample contained systems truly connected by a dense gaseous filament.

We also computed the transverse hydrogen profile of the filament for the physically connected pairs with a 3D distance below 1 pMpc. After selecting the filamentary structure as described above, we defined the direction of the filament's spine, and computed the two highest density points below and above $0.5d_{3D}$. With this approach, we could account for filaments not perfectly aligned with the axis joining the two haloes, as done in our analysis of the transverse SB profile in the MUSE data. Knowing the orientation of the filament, we considered a cylinder along the spine direction with a radius of 130 pkpc, which we divided into different shells with a width of $\Delta r = 15$ pkpc. As above, we estimated the hydrogen density as the total gas mass contained in a given shell divided by the volume of the shell, after accounting for the hydrogen fraction X_H. The profile obtained is shown in Extended Data Fig. 6. From this result, we inferred that the physically connected pairs have a filamentary structure with a median hydrogen density of ~$10^{-2.8}$ cm^{-3} in the densest part along the filament's spine and that the density falls from the centre of the filament with an exponential decline radius of 40 ± 15 pkpc.

To compare more closely the MUSE observations with the results of simulations, we derived the SB maps assuming that the diffuse gas emission originated from recombinations and collisional excitation. For each gas resolution element, we calculated the emissivities from the equations

$$\epsilon_{Ly\alpha}^{rec} = \frac{h\nu_{Ly\alpha}}{4\pi}\alpha_{eff}(T)(1-\eta)^2 n_H^2, \qquad (2)$$

and

$$\epsilon_{Ly\alpha}^{coll} = \frac{h\nu_{Ly\alpha}}{4\pi}\gamma_{1s2p}(T)\eta(1-\eta)n_H^2, \qquad (3)$$

where h is Planck's constant and $\nu_{Ly\alpha}$ is the Lyα frequency. The emissivities depend on the squared number density of neutral hydrogen, n_H. Recombinations were calculated assuming a case A scenario with the temperature-dependent recombination coefficient $\alpha_{eff}(T)$ from ref. 53 and the collisional excitation coefficient $\gamma_{1s2p}(T)$ from ref. 54. Assuming ionization equilibrium, the neutral hydrogen fraction, $\eta = n_{HI}/n_H$, was calculated following Appendix A2 in ref. 55, as done within the simulation. The temperature of each cell gas was calculated assuming a perfect monoatomic gas from the internal energy u given by the simulation, using the relationship $T_{cell} = (\gamma - 1)\mu m_p u/k_B$, where $\gamma = 5/3$, $\mu = 4/(1 + 3X_H + 4X_H x_e)$ is the mean molecular weight calculated with the electron abundance x_e given by the simulation and k_B is Boltzmann's constant. We included only gas with densities $n_H < 0.1$ cm^{-3}, that is, outside the imposed equation of state. Owing to the presence of the quasars in our observations, we also considered a maximal fluorescence model to test their possible effect on the gas in the filaments, assuming that the ionizing sources were bright enough to fully ionize the surrounding medium. Therefore, we calculated the emissivity of the gas due to Lyα recombination radiation following a simplified relationship where η was assumed to be zero in equation (2) (see, for example, ref. 34). Finally, using the public package Py-SPHViewer[56], we integrated along the line of sight (assumed as z) the total emissivity to obtain the SB images of the selected pairs (see, for example, Fig. 4b).

Using the same approach as followed in our observations (see also Extended Data Fig. 2b), we measured the transverse SB profile using nine rectangular boxes for each pair up to a distance of 100 kpc on either side relative to the direction connecting the two haloes. Once again, the boxes could be positioned off-axis to that direction, ensuring the emission peak was at $R = 0$. To exclude the contribution from the CGM of the two main haloes (but leaving possible contributions from other embedded haloes), the length of each box encompassed only the projected filament region, defined by maintaining a distance of $0.25d_{2D}$ from each halo, which was similar to the transition radius measured in the MUDF. As both emission processes considered here depend on the density square, we explicitly tested the robustness of these predictions as a function of resolution, and we compared the results in three boxes of the IllustrisTNG simulation (TNG300-1, TNG100-1 and TNG50-1), covering a range of ~200 in volume and ~130 in mass. Applying the pair selection described above for TNG100-1 yielded 710 pairs below 1 pMpc in TNG300-1 and 24 in TNG50-1.

Extended Data Fig. 7 compares the median emission profile from both recombinations and collisional excitations (orange line), as well as considering only recombinations (blue line), along with the 16th and 84th percentiles. We observed that, on average, the result was not strongly sensitive at the different resolutions of TNG, which implies that the typical densities within the mildly overdense filaments are reasonably converged at these scales, a result also found in simulations of the Lyα forest. We also observed that the maximal fluorescence model produces a median SB profile that agrees remarkably well, within a mean factor of ~2, with the recombination model. Thus, the simulations predict that the mostly optically thin filaments have temperature-dependent coefficients and ionization fractions close to the maximal fluorescence conditions, which is a result similar to the simulation predictions in ref. 57, where the SB of the faintest pixels originates from low column-density material that is already highly ionized and emitting near its maximum. This analysis concludes that the SB maps are generally robust relative to the assumptions made.

When comparing the predicted profiles with the observational data points measured in the MUDF up to ~70 pkpc, for which the measurements exceeded the detection limit of the NB image, we observed that the maximal fluorescence and the recombination models lie below the observed SB. This indicates that the densities predicted by the simulations cannot be too high compared with real values as, otherwise, the simulated profiles would exceed the observed ones. Moreover, observations and simulations can be

brought into agreement by increasing recombination radiation by a factor of ~9 in the SB, that is, by requiring an increase in density by a factor of not more than ~3. Hence, the simulated densities cannot be much lower than the true values. Such a boost should also be considered a maximum correction that must be applied owing to the presence of additional photons from collisions. Indeed, when including collisional excitations, despite the more uncertain nature of this calculation due to the high sensitivity to temperature, the profile shifts upward, in particular in the inner ~25 pkpc. We also note that the $0.1\,cm^{-3}$ cut is quite stringent, as we explicitly tested that the denser and more neutral gas around ~0.1–$0.3\,cm^{-3}$ is a significant source of photons. Including that phase, we observed a good agreement between the SB level predicted by the simulations and the MUDF filament, with both profiles lying at $\sim 10^{-19}\,erg\,s^{-1}\,cm^{-2}\,arcsec^{-2}$ in the range $R \approx 20$–40 pkpc, reducing the flattening at larger radius. Our analysis also neglects scattering processes that can redistribute photons from regions of high to low SB. Byrohl and Nelson[44] quantify the effects of radiative transfer in the TNG simulation, and, at the SB level observed in the MUDF filament, the boost factor is ~2–3. Hence, discrepancies are not particularly concerning. Moreover, we observed that this analysis does not require the introduction of large clumping factors to explain the SB levels, which suggests that the already mostly ionized, optically thin filaments have a simpler density distribution, reasonably captured by the simulations as tested above. High-density clumps, as required in the bright large Lyα nebulae, would produce SB values that exceed the observed ones also by two orders of magnitudes[16]. Overall, this analysis implies a satisfactory agreement between the density predicted in the cold-dark-matter model and what is observed.

Furthermore, there is no special reason why the MUDF filament should align with the distribution median. Considering this aspect, we searched among the simulated SB profiles for a pair that resembles the MUDF system more closely. One such MUDF twin is shown in Fig. 4, where we see a transverse profile that matches the observations. Hence, filaments with observed characteristics comparable with the MUDF exist in the cold-dark-matter paradigm, and our study paves the way for further quantitative analysis of the properties of the cosmic web within our cosmological model.

Resources

This research made use of Astropy, a community-developed core Python package for astronomy[58–60], NumPy[61], SciPy[62] and Matplotlib[63].

Data availability

The Very Large Telescope data used in this work are available from the European Southern Observatory archive https://archive.eso.org/ either as raw data or phase 3 data products[64].

References

1. Frenk, C. S., White, S. D. M., Davis, M. & Efstathiou, G. The formation of dark halos in a universe dominated by cold dark matter. *Astrophys. J.* **327**, 507–525 (1988).
2. Cen, R., Miralda-Escudé, J., Ostriker, J. P. & Rauch, M. Gravitational collapse of small-scale structure as the origin of the Lyman-Alpha forest. *Astrophys. J. Lett.* **437**, L9–L12 (1994).
3. Lukić, Z. et al. The Lyman α forest in optically thin hydrodynamical simulations. *Mon. Not. R. Astron. Soc.* **446**, 3697–3724 (2015).
4. Peacock, J. A. et al. A measurement of the cosmological mass density from clustering in the 2dF Galaxy Redshift Survey. *Nature* **410**, 169–173 (2001).
5. Tempel, E. et al. Detecting filamentary pattern in the cosmic web: a catalogue of filaments for the SDSS. *Mon. Not. R. Astron. Soc.* **438**, 3465–3482 (2014).
6. Rauch, M. The Lyman alpha forest in the spectra of QSOs. *Annu. Rev. Astron. Astrophys.* **36**, 267–316 (1998).
7. Haardt, F. & Madau, P. Radiative transfer in a clumpy universe. IV. New synthesis models of the cosmic UV/X-ray background. *Astrophys. J.* **746**, 125 (2012).
8. Gould, A. & Weinberg, D. H. Imaging the forest of Lyman limit systems. *Astrophys. J.* **468**, 462–468 (1996).
9. Bacon, R. et al. The MUSE second-generation VLT instrument. In *Proc. Ground-based and Airborne Instrumentation for Astronomy III* Vol. 7735 (eds McLean, I. S. et al.) 773508 (SPIE, 2010).
10. Morrissey, P. et al. The Keck Cosmic Web Imager integral field spectrograph. *Astrophys. J.* **864**, 93 (2018).
11. Martin, D. C. et al. Intergalactic medium emission observations with the Cosmic Web Imager. I. The circum-QSO medium of QSO 1549+19, and evidence for a filamentary gas inflow. *Astrophys. J.* **786**, 106 (2014).
12. Husband, K., Bremer, M. N., Stanway, E. R. & Lehnert, M. D. Dissecting the complex environment of a distant quasar with MUSE. *Mon. Not. R. Astron. Soc.* **452**, 2388–2395 (2015).
13. Borisova, E. et al. Ubiquitous giant Lyα nebulae around the brightest quasars at z~3.5 revealed with MUSE. *Astrophys. J.* **831**, 39 (2016).
14. Arrigoni Battaia, F. et al. QSO MUSEUM I: a sample of 61 extended Ly α-emission nebulae surrounding z~3 quasars. *Mon. Not. R. Astron. Soc.* **482**, 3162–3205 (2019).
15. Fossati, M. et al. MUSE analysis of gas around galaxies (MAGG) – III. The gas and galaxy environment of z=3–4.5 quasars. *Mon. Not. R. Astron. Soc.* **503**, 3044–3064 (2021).
16. Cantalupo, S., Arrigoni-Battaia, F., Prochaska, J. X., Hennawi, J. F. & Madau, P. A cosmic web filament revealed in Lyman-α emission around a luminous high-redshift quasar. *Nature* **506**, 63–66 (2014).
17. Umehata, H. et al. Gas filaments of the cosmic web located around active galaxies in a protocluster. *Science* **366**, 97–100 (2019).
18. Bacon, R. et al. The MUSE Extremely Deep Field: the cosmic web in emission at high redshift. *Astron. Astrophys.* **647**, A107 (2021).
19. Cai, Z. et al. Keck/Palomar Cosmic Web Imagers reveal an enormous Lyα nebula in an extremely overdense quasi-stellar object pair field at z=2.45. *Astrophys. J. Lett.* **861**, L3 (2018).
20. Arrigoni Battaia, F. et al. Discovery of intergalactic bridges connecting two faint z~3 quasars. *Astron. Astrophys.* **631**, A18 (2019).
21. Herenz, E. C., Hayes, M. & Scarlata, C. Deciphering the Lyman α blob 1 with deep MUSE observations. *Astron. Astrophys.* **642**, A55 (2020).
22. Martin, D. C. et al. Extensive diffuse Lyman-α emission correlated with cosmic structure. *Nat. Astron.* **7**, 1390–1401 (2023).
23. Revalski, M. et al. The MUSE Ultra Deep Field (MUDF). III. Hubble Space Telescope WFC3 grism spectroscopy and imaging. *Astrophys. J. Suppl. Ser.* **265**, 40 (2023).
24. Fossati, M. et al. The MUSE Ultra Deep Field (MUDF). II. Survey design and the gaseous properties of galaxy groups at 0.5<z<1.5. *Mon. Not. R. Astron. Soc.* **490**, 1451–1469 (2019).
25. Lusso, E. et al. The MUSE Ultra Deep Field (MUDF) - I. Discovery of a group of Lyα nebulae associated with a bright z≈3.23 quasar pair. *Mon. Not. R. Astron. Soc.* **485**, L62–L67 (2019).
26. Rosdahl, J. & Blaizot, J. Extended Lyα emission from cold accretion streams. *Mon. Not. R. Astron. Soc.* **423**, 344–366 (2012).
27. Rahmati, A. et al. The distribution of neutral hydrogen around high-redshift galaxies and quasars in the EAGLE simulation. *Mon. Not. R. Astron. Soc.* **452**, 2034–2056 (2015).
28. Kereš, D., Katz, N., Weinberg, D. H. & Davé, R. How do galaxies get their gas? *Mon. Not. R. Astron. Soc.* **363**, 2–28 (2005).
29. Dekel, A. et al. Cold streams in early massive hot haloes as the main mode of galaxy formation. *Nature* **457**, 451–454 (2009).
30. Rauch, M., Becker, G. D. & Haehnelt, M. G. Observational aspects of galactic accretion at redshift 3.3. *Mon. Not. R. Astron. Soc.* **455**, 3991–3999 (2016).

31. Daddi, E. et al. Three Lyman-α-emitting filaments converging to a massive galaxy group at z=2.91: discussing the case for cold gas infall. *Astron. Astrophys.* **649**, A78 (2021).

32. Mackenzie, R. et al. Revealing the impact of quasar luminosity on giant Lyα nebulae. *Mon. Not. R. Astron. Soc.* **502**, 494–509 (2021).

33. Nielsen, N. M. et al. An emission map of the disk–circumgalactic medium transition in starburst IRAS 08339+6517. *Nat. Astron.* **8**, 1602–1609 (2024).

34. de Beer, S. et al. Resolving the physics of quasar Lyα nebulae (RePhyNe): I. Constraining quasar host halo masses through circumgalactic medium kinematics. *Mon. Not. R. Astron. Soc.* **526**, 1850–1873 (2023).

35. Wilde, M. C. et al. CGM² + CASBaH: the mass dependence of H I Lyα–galaxy clustering and the extent of the CGM. *Astrophys. J.* **948**, 114 (2023).

36. Kikuchihara, S. et al. SILVERRUSH. XII. Intensity mapping for Lyα emission extending over 100–1000 comoving kpc around z~2–7 LAEs with Subaru HSC-SSP and CHORUS data. *Astrophys. J.* **931**, 97 (2022).

37. Lujan Niemeyer, M. et al. Surface brightness profile of Lyman-α halos out to 320 kpc in HETDEX. *Astrophys. J.* **929**, 90 (2022).

38. Guo, Y. et al. Median surface-brightness profiles of Lyman-α haloes in the MUSE Extremely Deep Field. *Astron. Astrophys.* **688**, A37 (2024).

39. Arrigoni Battaia, F., Hennawi, J. F., Cantalupo, S. & Prochaska, J. X. The stacked LYα emission profile from the circum-galactic medium of z~2 quasars. *Astrophys. J.* **829**, 3 (2016).

40. Izquierdo-Villalba, D. et al. The build-up of pseudo-bulges in a hierarchical universe. *Mon. Not. R. Astron. Soc.* **488**, 609–632 (2019).

41. Izquierdo-Villalba, D. et al. From galactic nuclei to the halo outskirts: tracing supermassive black holes across cosmic history and environments. *Mon. Not. R. Astron. Soc.* **495**, 4681–4706 (2020).

42. Lusso, E. et al. The MUSE Ultra Deep Field (MUDF). IV. A pair of X-ray weak quasars at the heart of two extended Lyα nebulae. *Mon. Not. R. Astron. Soc.* **525**, 4388–4404 (2023).

43. Nelson, D. et al. The IllustrisTNG simulations: public data release. *Comput. Astrophys. Cosmol.* **6**, 2 (2019).

44. Byrohl, C. & Nelson, D. The cosmic web in Lyman-alpha emission. *Mon. Not. R. Astron. Soc.* **523**, 5248–5273 (2023).

45. Cantalupo, S. et al. The large- and small-scale properties of the intergalactic gas in the Slug Ly α nebula revealed by MUSE He II emission observations. *Mon. Not. R. Astron. Soc.* **483**, 5188–5204 (2019).

46. Lofthouse, E. K. et al. MUSE Analysis of Gas around Galaxies (MAGG) – I: survey design and the environment of a near pristine gas cloud at z ≈ 3.5. *Mon. Not. R. Astron. Soc.* **491**, 2057–2074 (2019).

47. Weilbacher, P. M. et al. The MUSE Data Reduction Pipeline: Status after preliminary acceptance Europe. In *Astronomical Data Analysis Software and Systems XXIII* Vol. 485 (eds Manset, N. & Forshay, P.) 451–454 (Astronomical Society of the Pacific, 2014).

48. Foreman-Mackey, D., Hogg, D. W., Lang, D. & Goodman, J. emcee: the MCMC hammer. *Publ. Astron. Soc. Pac.* **125**, 306–312 (2013).

49. Arrigoni Battaia, F., Obreja, A., Costa, T., Farina, E. P. & Cai, Z. The luminosity–area relation of z > 2 quasars' Lyα Nebulae. *Astrophys. J. Lett.* **952**, L24 (2023).

50. Hennawi, J. F. & Prochaska, J. X. Quasars probing quasars. IV. Joint constraints on the circumgalactic medium from absorption and emission. *Astrophys. J.* **766**, 58 (2013).

51. Henriques, B. M. B. et al. Galaxy formation in the Planck cosmology – I. Matching the observed evolution of star formation rates, colours and stellar masses. *Mon. Not. R. Astron. Soc.* **451**, 2663–2680 (2015).

52. Springel, V. et al. Simulations of the formation, evolution and clustering of galaxies and quasars. *Nature* **435**, 629–636 (2005).

53. Hui, L. & Gnedin, N. Y. Equation of state of the photoionized intergalactic medium. *Mon. Not. R. Astron. Soc.* **292**, 27–42 (1997).

54. Scholz, T. T. & Walters, H. R. J. Collisional rates and cooling within atomic hydrogen plasmas. *Astrophys. J.* **380**, 302–306 (1991).

55. Rahmati, A., Pawlik, A. H., Raičević, M. & Schaye, J. On the evolution of the H I column density distribution in cosmological simulations. *Mon. Not. R. Astron. Soc.* **430**, 2427–2445 (2013).

56. Benitez-Llambay, A. py-sphviewer: Py-sphviewer v.1.0.0. *Zenodo* https://doi.org/10.5281/zenodo.21703 (2015).

57. Kollmeier, J. A. et al. Lyα emission from cosmic structure. I. Fluorescence. *Astrophys. J.* **708**, 1048–1075 (2010).

58. Astropy Collaboration et al. Astropy: a community Python package for astronomy. *Astron. Astrophys.* **558**, A33 (2013).

59. Astropy Collaboration et al. The Astropy Project: building an open-science project and status of the v2.0 core package. *Astron. J.* **156**, 123 (2018).

60. Astropy Collaboration et al. The Astropy Project: sustaining and growing a community-oriented open-source project and the latest major release (v5.0) of the core package. *Astrophys. J.* **935**, 167 (2022).

61. Harris, C. R. et al. Array programming with NumPy. *Nature* **585**, 357–362 (2020).

62. Virtanen, P. et al. SciPy 1.0: fundamental algorithms for scientific computing in Python. *Nat. Methods* **17**, 261–272 (2020).

63. Hunter, J. D. Matplotlib: a 2D graphics environment. *Comput. Sci. Eng.* **9**, 90–95 (2007).

64. Fumagalli, M. Exploring an uncharted portion of the universe with a MUSE ultra deep field. *ESO Archive* https://doi.org/10.18727/archive/84 (2023).

Acknowledgements

Author contributions

D.T. analysed the observations and was the main author of the manuscript. M. Fumagalli coordinated the MUDF programme, participated in the data analysis, and coauthored the manuscript. M. Fossati reduced and analysed the observations and participated in the analysis and manuscript writing. A.B.-L. contributed to the simulation analysis and D.I.-V. created and provided the SAM light cone and contributed to the analysis. All coauthors participated in preparing the manuscript.

Competing interests

The authors declare no competing interests.

Additional information

[1]Physics Department, Università degli Studi di Milano-Bicocca, Milan, Italy. [2]Osservatorio Astronomico di Trieste, INAF, Trieste, Italy. [3]Osservatorio
Astronomico di Brera, INAF, Milan, Italy. [4]INFN, Sezione di Milano-Bicocca Piazza della Scienza 3, Milan, Italy. [5]Max-Planck-Institut für Astrophysik,
Garching bei München, Germany. [6]Space Telescope Science Institute, Baltimore, MD, USA. [7]Donostia International Physics Center (DIPC), San Sebastián,
Spain. [8]IKERBASQUE, Basque Foundation for Science, Bilbao, Spain. [9]Kapteyn Astronomical Institute, Rijksuniversiteit Groningen, Groningen, the
Netherlands. [10]Scuola Normale Superiore, Pisa, Italy. [11]Institute for Fundamental Physics of the Universe, IFPU, Trieste, Italy. [12]IUCAA, Ganeshkind, India.
[13]Dipartimento di Fisica e Astronomia, Università di Firenze, Florence, Italy. [14]Osservatorio Astrofisico di Arcetri, INAF, Florence, Italy. [15]European Southern
Observatory, Garching bei München, Germany. [16]Aix Marseille Université, CNRS, Marseilles, France. [17]Department of Physics and Astronomy, Johns
Hopkins University, Baltimore, MD, USA. [18]Department of Astronomy, MongManWai Building, Tsinghua University, Beijing, People's Republic of China.
[19]Centre for Extragalactic Astronomy, Department of Physics, Durham University, Durham, UK. ✉e-mail: d.tornotti@campus.unimib.it;
michele.fumagalli@unimib.it
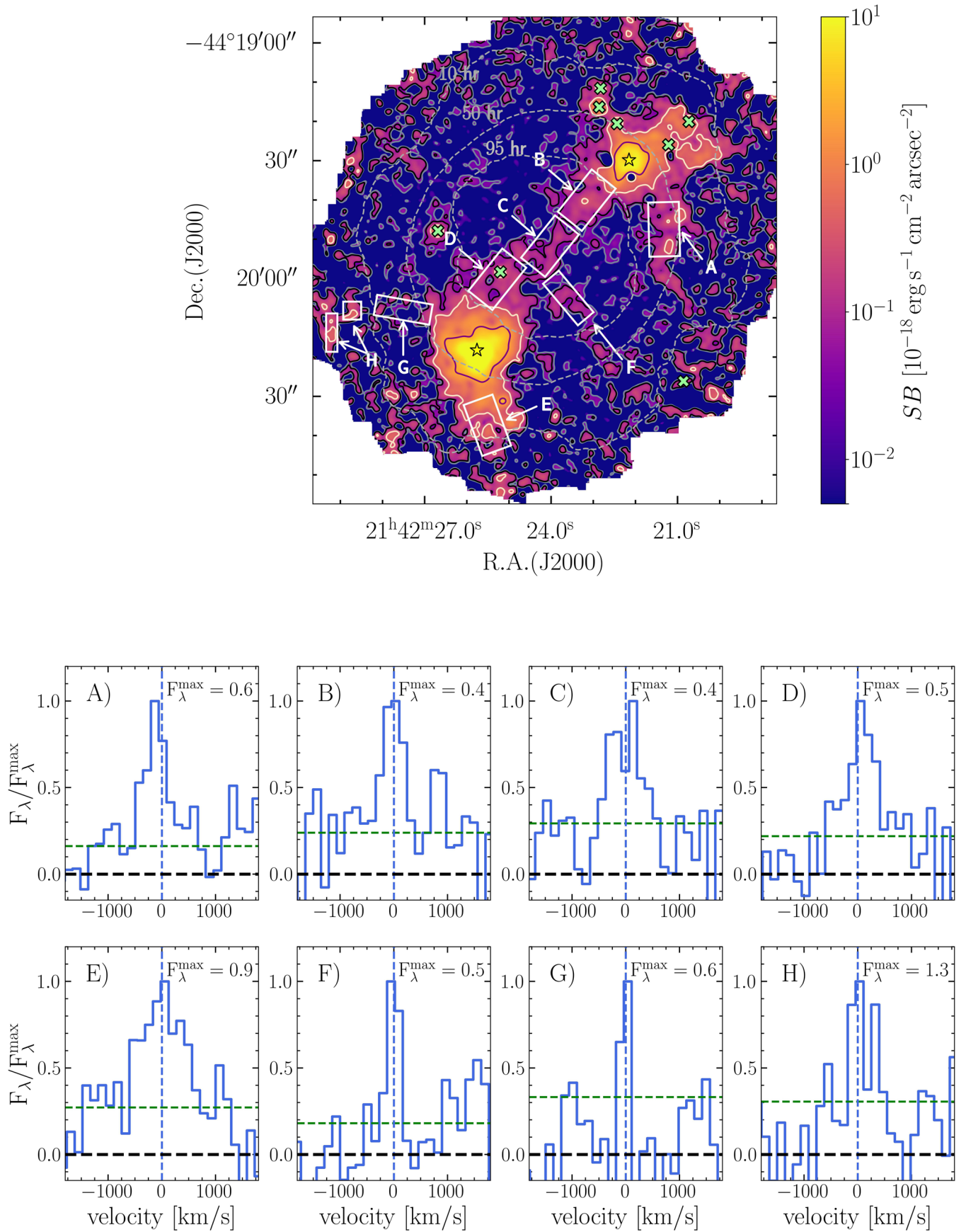
**Extended Data Fig. 1 | See next page for caption.**

Extended Data Fig. 1 | Lyα emission image with noise and mean spectra. Top, Optimally extracted Lyα image on top of three collapsed wavelength layers at the central wavelength of the quasar nebula emission. The contour levels are 0.02, 0.06, 0.3 and 2×10^{-18} erg cm^{-2} s^{-1} arcsec^{-2} (light-grey, black, light-orange, purple). The green crosses represent the position of the detected Lyα emitters within 1500 km s^{-1} from the average redshift of the two quasars. Bottom, Normalized mean spectra in velocity space extracted from the white boxes labeled from A to H in (a). The F_{λ}^{max} are the maximum flux density values used to normalize the mean spectra in units of 10^{-21} erg s^{-1} cm^{-2} Å^{-1}. The vertical dashed blue line represents the zero velocity reference calculated from the first moment of the line, and the horizontal dashed green line represents the 1σ noise level of the spectrum.
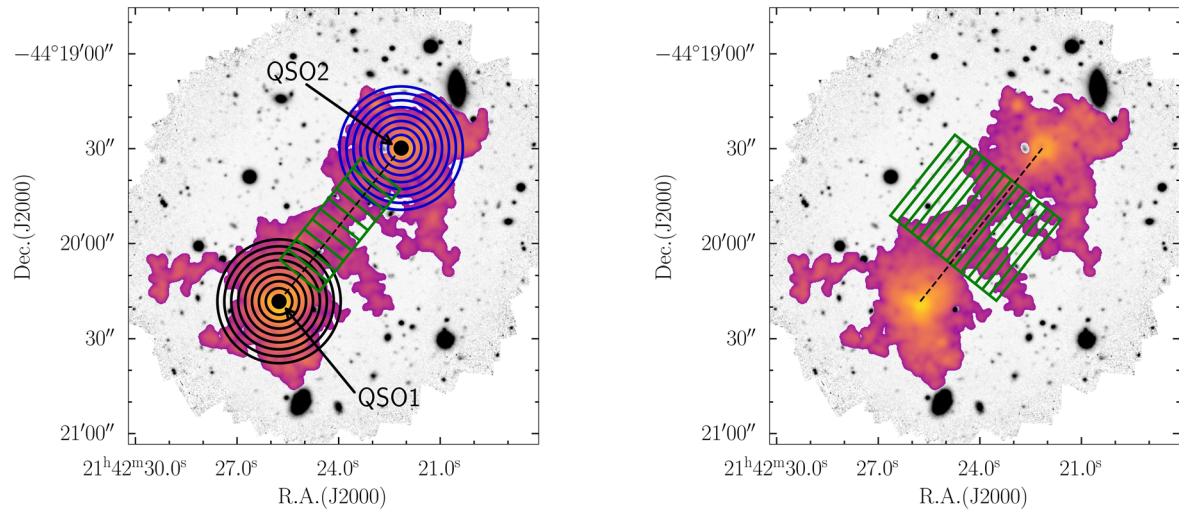
Extended Data Fig. 2 | Extraction apertures for surface brightness profiles of nebulae and filament. Left, Extraction apertures (black annuli for Nebula 1, blue annuli for Nebula 2, and green boxes for the filament) used to extract the surface brightness profiles, superimposed to the Lyα emission map, included solely for illustrative purposes. The two black dots mark a ≈ 15 pkpc radius where the quasar's PSF residuals dominate the signal. QSO1 and QSO2 are indicated by the two black arrows, respectively. Right, Same as Left but for the transverse surface brightness profile. In the background of both images, shown in grey, is a white-light image of the region imaged by MUSE.
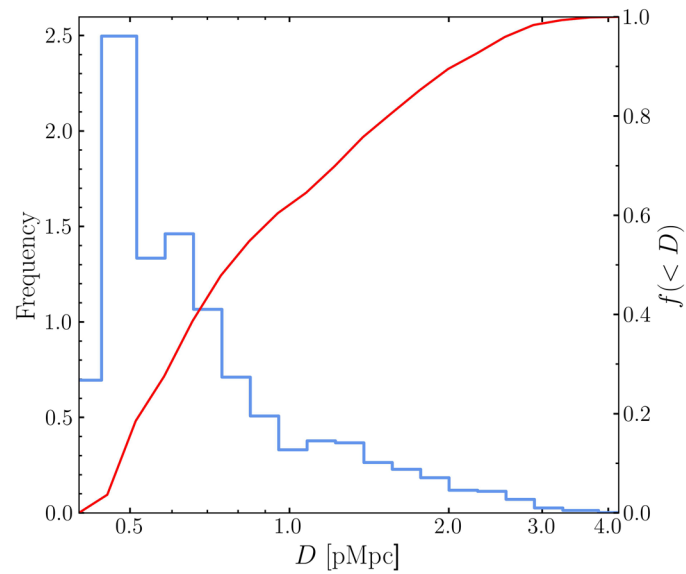
Extended Data Fig. 3 | 3D distance distribution of selected pairs. The frequency distribution of the 3D physical distance between each selected pair (blue histogram) and the corresponding cumulative probability function (red line) are shown. The distribution is normalized to the number of selected pairs. A large fraction of MUDF pair twins are found to be sufficiently close to be interacting in some form.
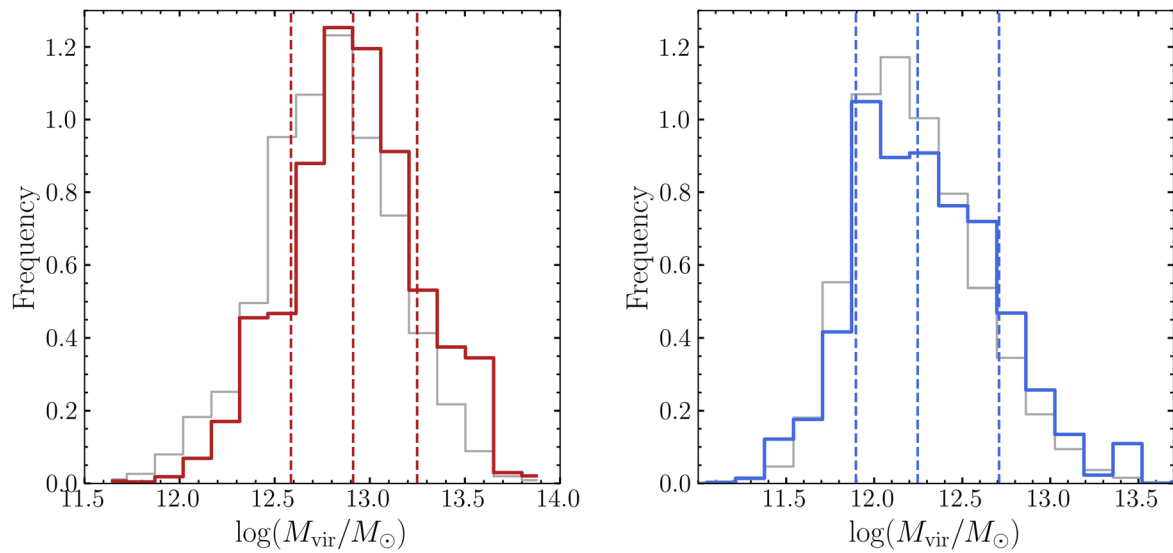
Extended Data Fig. 4 | Virial halo mass distributions for bright and faint quasars. Left, The virial halo mass distribution in the SAM of the bright quasars $(\log(L_{bol}/\mathrm{erg\,s^{-1}}) = 47.3 \pm 0.3)$ selected across the full-sky is shown in grey. The red curve represents the distribution of bright quasars among the selected pairs that mimic the MUDF system in the sky. (**b**) Right, Same as Left but for the faint quasars $(\log(L_{bol}/\mathrm{erg\,s^{-1}}) = 46.3 \pm 0.3)$. In blue, the subsample resembling the MUDF system in the sky. All distributions are normalized to the bin width and the number of bright and faint sources obtained from their respective selections. Dashed lines indicate the mean values along with the 16th and 84th percentiles.
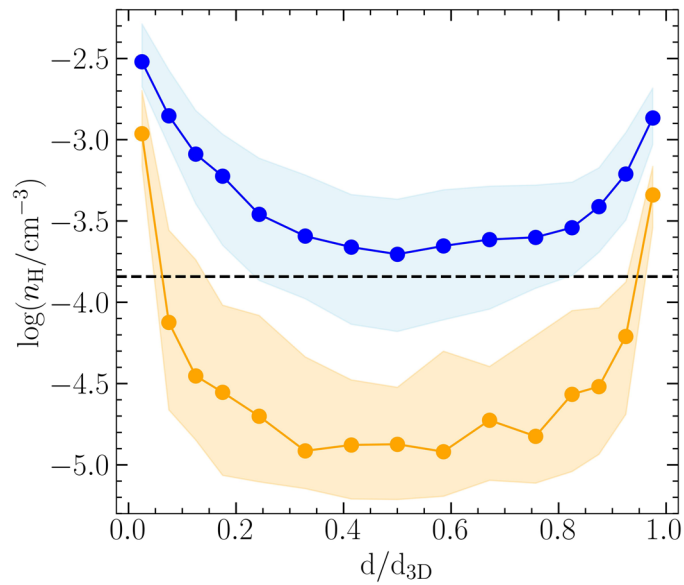
Extended Data Fig. 5 | Median hydrogen density profiles for close and distant pairs. The median hydrogen density profile along the filament of the selected close and distant pairs separated by a 3D distance of < 1 pMpc (blue line) and > 2 pMpc (orange line), are shown. Both profiles are plotted as a function of the normalized 3D physical distance between the two halos. The shaded regions represent the 16th and 84th percentiles of the profiles distribution. The black dashed lines represent ten times the hydrogen critical density of the Universe at this redshift, the threshold used to compare the properties of the two subsamples.
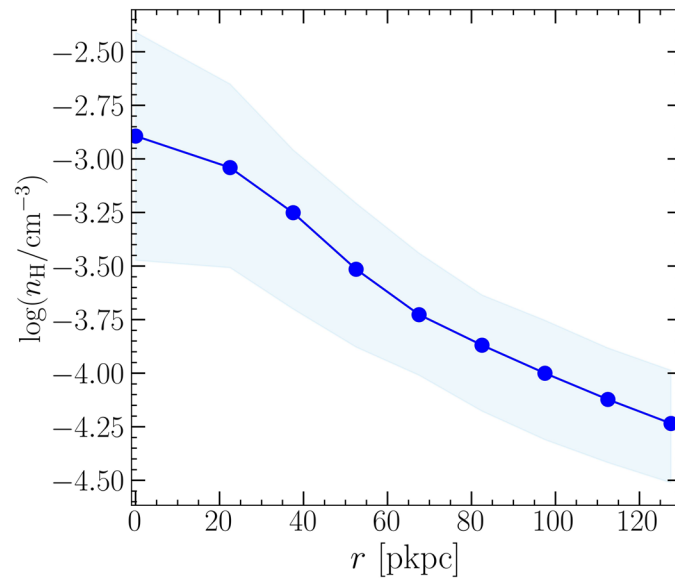
Extended Data Fig. 6 | Transverse median hydrogen density profile for physically connected pairs. The transverse median hydrogen density profile of the physically connected pairs separated by a 3D distance < 1 pMpc is shown. The sky-blue colored region represents the 16th and 84th percentiles of the profiles distribution.
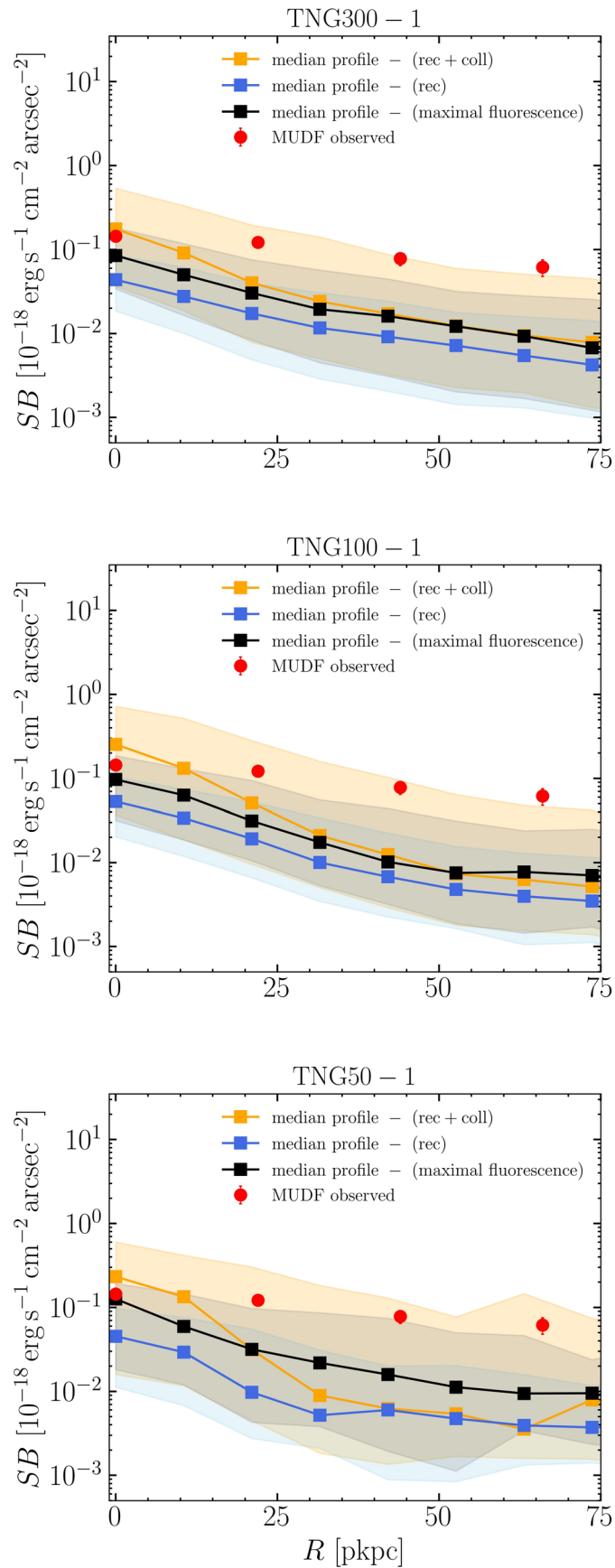
Extended Data Fig. 7 | See next page for caption.

Extended Data Fig. 7 | Transverse median surface brightness profiles for physically connected pairs. The median transverse surface brightness profiles of the selected pairs with a 3D distance below 1 pMpc in TNG300-1, TNG100-1 and TNG50-1 are shown, respectively. The blue line represents the emission contribution from recombinations only, while the orange line represents both recombinations and collisional excitations. The emission contribution from the maximal fluorescence model is also shown as a black line. The red points represent the measured data and their errors for the transverse surface brightness profile in MUDF. The shaded regions denote the 16th and 84th percentiles of the profile distributions.